JOURNAL OF COMPUTATIONAL PHYSICS 109, 133–149 (1993)

A Spectral Element Basin Model for the Shallow Water Equations

HONG MA*

Department of Atmospheric, Oceanic and Space Sciences and Laboratory for Scientific Computing, The University of Michigan, Ann Arbor, Michigan 48109

Received January 10, 1992; revised December 16, 1992

A spectral element model is built for the shallow water equations in complex geometry. It is proved to be an efficient computational model in solving oceanic problems. In particular, the equatorial Rossby modon's reflection process is simulated.

1. INTRODUCTION

In the world of scientific computation, three numerical methods are most frequently used: the finite difference method, the spectral method, and the finite element method. Through decades of development, both in theory and in application, these three methods have almost been perfected.

The finite difference method has been around the longest and is still popular because of its simplicity. In fact, if precision is not the crucial issue, the finite difference method is indeed very efficient with regard to programming and computational cost. The application of the finite difference method in geophysical fluid dynamics can be tracked back to some 70 years ago when L. F. Richardson did the first numerical weather prediction [16]. Even though the first weather forecast turned out to be unsuccessful, it was a milestone in meteorology nevertheless. Today's atmospheric general circulation models (GCMs), much more accurate of course, are still using the finite difference method, mostly in the vertical spatial direction. The simulation of oceanic circulation began in the early 1960s [3]. Most of the oceanic GCMs use the finite difference method in all three spatial directions.

The spectral method is a high order weighted residual method. It is also known as the p-type weighted residual method. Unlike the finite element method, the trial functions of the spectral method are global, so it is usually applied to regular geometrical problems with smooth solutions. The spectral method is famous for its efficiency for achieving high precision. It has been estimated [2] that in order to obtain 1% accuracy for a wave-like solution, 40 grid points per wavelength are needed for the second-order finite difference method, but only 3.5 collocation points per wave length are needed for the Chebyshev spectral method. Therefore, the spectral method is about 10 times more efficient than the finite difference method in storage aspect alone (in one dimension). Peyret and Taylor [15] compared the finite difference method with the spectral method and found that the spectral method was at least 10 times faster than the finite difference method for the same accuracy in the vortex problem they solved. Haidvogel *et al.* [7] also demonstrated the overwhelming advantage of the spectral method over the finite difference and the finite element methods in solving the vorticity equation problem in an unbounded ocean.

However, the spectral method has its own limitations. For instance, the grid resolution is not uniform and it increases drastically toward the boundaries of the computational domain. This imposes a severe limitation on the maximum time step when solving initial value problems via an explicit time marching scheme [6]. Therefore, we often use implicit methods in conjunction with spectral algorithms. Unfortunately, these implicit schemes are not terribly efficient either, because the matrices in the spectral method are full matrices, unlike the narrowly banded matrices of the finite difference and the finite element methods. Some spectral matrices may be solved more efficiently by applying different kinds of preconditionings and multi-grid techniques [2].

The finite element method is a low order, h-type weighted residual method. It has been widely applied to many mechanical engineering fields, especially in solid mechanics, because of its extreme geometrical flexibility. There are some applications of the finite element method in coastal engineering where complicated coastlines often have to be

* Present address: Department of Applied Science, Bldg. 515, Brookhaven National Laboratory, Upton, Long Island, NY 11973.

0021-9991/93 $5.00

approximated either by straight lines or zigzag lines in order to use spectral or finite difference methods. With finite elements, curvy coastlines can be approximated rather well without a lot of computational effort [18]. The drawback of the finite element method is that it is a low order method. Like finite difference methods, the finite element method converges slowly as the number of the elements is increased.

The spectral element method is a combination of both the spectral and the finite element methods. It was first introduced by Patera [14]. The spectral element method is also called the "p-type finite element" method, or the h–p type weighted residual method. Like the spectral method, it uses high order polynomials as trial functions, but like the finite element method, it decomposes the computational domain into many elements and defines local trial functions. The hybrid character of the spectral element method enables it to overcome the shortcomings of both the spectral method and the finite element method but still retain their advantages. Since the trial functions of the spectral element method are local, it can handle complex geometry easily [9]. On the other hand, it is still a high order weighted residual method, so the exponential convergence rate is achieved as the degree of the polynomials in each element is increased. The main difference between the spectral element method and the spectral multi-domain method is that the C^0 and C^1 boundary conditions at the interface of the elements have to be explicitly enforced by the spectral multi-domain method. The spectral element method, by contrast, uses the variational principle to guarantee C^0 and C^1 (weakly) continuity at the interface [12], which results in a much simpler and more natural approach than the non-variational method; therefore, parallel algorithms can be conveniently implemented [5]. Over the past seven years of development and application, mostly in mechanical engineering fields, the spectral element method has been proved to be a very promising numerical method. In geophysical fluid dynamics, however, the application of the spectral element method is only in a very early stage [10, 11].

The purpose of the present work is to build a spectral element model for the shallow water equations which have a special position in studying the behavior of the thin layer of fluid on the earth's surface, i.e., the atmosphere and ocean. The spectral element interpolation schemes used here are similar to those developed by Patera [14] and Ronquist [17]. However, instead of using a semi-implicit time marching scheme as proposed by [14, 17], we found that with the horizontal eddy viscosity range for oceanic applications, it is more efficient to use a fully explicit scheme for the current spectral element shallow water equation model. In the case of the Navier–Stokes equations or the Stokes equations, matrix iterations or inversions can be expensive because the related matrices have dense blocks due to the spectral element formulation. In the case of the shallow water equations, however, when a fully explicit time marching scheme is used, the matrix needed to be inverted in the current model is diagonal! The present work showed convincing evidence that the spectral element model for the shallow water equations can provide not only good spatial resolution and geometrical flexibility, but also affordability for long-range time dependent simulations which are needed in climate related studies.

2. MODEL FORMULATION

2.1. *Governing Equations*

If the horizontal eddy viscosity is included, the shallow water equations are of the form

$$\frac{\partial u}{\partial t}+u\frac{\partial u}{\partial x}+v\frac{\partial u}{\partial y}-fv=-g\frac{\partial h}{\partial x}+A_H\left(\frac{\partial^2 u}{\partial x^2}+\frac{\partial^2 u}{\partial y^2}\right) \tag{2.1}$$

$$\frac{\partial v}{\partial t}+u\frac{\partial v}{\partial x}+v\frac{\partial v}{\partial y}+fu=-g\frac{\partial h}{\partial y}+A_H\left(\frac{\partial^2 v}{\partial x^2}+\frac{\partial^2 v}{\partial y^2}\right) \tag{2.2}$$

$$\frac{\partial}{\partial t}+\frac{\partial}{\partial x}[(H+h)u]+\frac{\partial}{\partial y}[(H+h)v]=0, \tag{2.3}$$

where h is the surface displacement, g is the gravitational acceleration, H is the mean depth of the fluid, f is the Coriolis parameter calculated through the β plane approximation ($f=f_0+\beta y$), and A_H is the horizontal eddy viscosity parameter.

If the equatorial nondimensionalization scales are used, the variables in the shallow water equations on an equatorial β plane can be nondimensionalized as

$$(x, y)=E^{-1/4}a(x', y')=L(x', y') \tag{2.4}$$

$$t=E^{1/4}(2\Omega)^{-1}t'=Tt' \tag{2.5}$$

$$(u, v)=(gH_0)^{1/2}(u', v')=U(u', v') \tag{2.6}$$

$$h=H_0h' \tag{2.7}$$

$$f=\beta y=2\Omega E^{-1/4}y', \tag{2.8}$$

where the Lamb number $E=4\Omega^2a^2(gH_0)^{-1}$, a is the radius of the earth, $\Omega=2\pi\ day^{-1}$, and H_0 can be either the mean depth of the ocean for a barotropic model, or the so-called "equivalent depth" for a reduced gravity model. If we choose the equivalent depth $H_0=40$ cm, then $L=295$ km and $T=1.71$ days.

Substituting the above nondimensional variables into Eqs. (2.1)–(2.3) and omitting the primes, we obtain the nondimensionalized shallow water equations

$$\frac{\partial u}{\partial t}+u\frac{\partial u}{\partial x}+v\frac{\partial u}{\partial y}-yv=-\frac{\partial h}{\partial x}+\frac{1}{\mathrm{R_e}}\left(\frac{\partial^2 u}{\partial x^2}+\frac{\partial^2 u}{\partial y^2}\right) \tag{2.9}$$

$$\frac{\partial v}{\partial t}+u\frac{\partial v}{\partial x}+v\frac{\partial v}{\partial y}+yu=-\frac{\partial h}{\partial y}+\frac{1}{R_e}\left(\frac{\partial^2 v}{\partial x^2}+\frac{\partial^2 v}{\partial y^2}\right) \tag{2.10}$$

$$\frac{\partial h}{\partial t}+\frac{\partial}{\partial x}[u(1+h)]+\frac{\partial}{\partial y}[v(1+h)]=0, \tag{2.11}$$

where R_e is the Reynolds number defined as $1/R_e = A_H(UL)^{-1}$.

For an ocean basin model, we assume no slip and no normal flow boundary conditions, namely,

$$u(x, y, t)=v(x, y, t)=0 \qquad (x, y)\in\partial\Omega, \tag{2.12}$$

where $\partial\Omega$ is the boundary of the computational domain Ω.

If we neglect the effect of the meridional boundaries, the above rigid boundary conditions may be substituted by semi-periodic boundary conditions. In this case, the northern and southern boundaries are usually assumed to be rigid, but the channel is self-connected (periodic) in the zonal direction.

2.2. *Weak Form*

Assuming $(u, v, h)\in\mathscr{H}^1(\Omega)$ (Sobolev space) and their test functions $(\bar{u}, \bar{v}, \bar{h})\in\mathscr{H}^1(\Omega)$, then by multiplying the test functions through the corresponding equations in Eqs. (2.9)–(2.11) and integrating, the weak form of the shallow water equation system is obtained as

$$\int_\Omega \frac{\partial u}{\partial t}\bar{u}\,d_\Omega = -\int_\Omega\left(u\frac{\partial u}{\partial x}+v\frac{\partial u}{\partial y}-yv+\frac{\partial h}{\partial x}\right)\bar{u} + \frac{1}{R_e}\left(\frac{\partial u}{\partial x}\frac{\partial \bar{u}}{\partial x}+\frac{\partial u}{\partial y}\frac{\partial \bar{u}}{\partial y}\right)d\Omega \tag{2.13}$$

$$\int_\Omega \frac{\partial v}{\partial t}\bar{v}\,d_\Omega = -\int_\Omega\left(u\frac{\partial v}{\partial x}+v\frac{\partial v}{\partial y}+yu+\frac{\partial h}{\partial y}\right)\bar{v} + \frac{1}{R_e}\left(\frac{\partial v}{\partial x}\frac{\partial \bar{v}}{\partial x}+\frac{\partial v}{\partial y}\frac{\partial \bar{v}}{\partial y}\right)d\Omega \tag{2.14}$$

$$\int_\Omega \frac{\partial h}{\partial t}\bar{h}\,d\Omega=\int_\Omega u(1+h)\frac{\partial \bar{h}}{\partial x}+v(1+h)\frac{\partial \bar{h}}{\partial y}\,d\Omega. \tag{2.15}$$

The Dirichlet boundary condition (2.12) is used in deriving the above equations, which means that $(u, v)\in\mathscr{H}^1_0(\Omega)$ and $(\bar{u}, \bar{v})\in\mathscr{H}^1_0(\Omega)$. $\mathscr{H}^1_0(\Omega)$ is defined by $\mathscr{H}^1_0(\Omega)=\{v\in\mathscr{H}^1_0(\Omega)\mid v\in\mathscr{L}^2(\Omega), v_x\in\mathscr{L}^2(\Omega), v_y\in\mathscr{L}^2(\Omega), v(\partial\Omega)=0\}$.

The task of the variational method is to find $(u, v)\in\mathscr{H}^1_0(\Omega)$ and $h\in\mathscr{H}^1(\Omega)$ such that the residuals of (2.13)–(2.15) are minimized for all $(\bar{u}, \bar{v})\in\mathscr{H}^1_0(\Omega)$ and $\bar{h}\in\mathscr{H}^1(\Omega)$.

2.3. *Domain Decomposition and Local Coordinate Transformation*

Let Ω be an arbitrary two-dimensional geometrical domain and let Ω be decomposed into K elements Ω_e, $e=1, 2, ..., K$, in such a way that Ω_e has the following properties:

- $\bigcup_{e=1}^{K}\Omega_e=\Omega$;
- $\Omega_i\cap\Omega_j=\partial\Omega_{ij}$ if Ω_i and Ω_j are connected and $\partial\Omega_{ij}$ is their common boundary.

Let $\mathscr{G}$ be a continuous one-to-one mapping such that $\mathscr{G}(\Omega)=\hat{\Omega}$. Then under mapping $\mathscr{G}$, there is a corresponding element decomposition on $\hat{\Omega}$ and its elements $\hat{\Omega}_e$ also satisfy the listed connection properties. In addition, $\hat{\Omega}_e$ are assumed to be rectangles, which can be achieved by properly choosing $\mathscr{G}$. There are developed techniques to deal with domain mapping problems. In particular, the so-called isoparametric method, which is widely used in the finite element method, has also been successfully applied in the spectral element method [9]. The isoparametric algorithm is going to be discussed in the next section.

Now each element $\hat{\Omega}_e$, which is a rectangle $[a^e_l, a^e_r]\times[a^e_b, a^e_t]$, is ready to be mapped onto a square, $\Lambda^2=[-1, 1]^2$, by

$$\xi=\frac{2}{|a^e_r-a^e_l|}(\hat{x}-a^e_l)-1, \qquad e=1, 2, ..., K. \tag{2.16}$$

$$\eta=\frac{2}{|a^e_t-a^e_b|}(\hat{y}-a^e_b)-1, \qquad e=1, 2, ..., K. \tag{2.17}$$

where $(\hat{x}, \hat{y})$ are the coordinates of a collocation point on $\hat{\Omega}_e$ and (ξ, η) are the corresponding local coordinates on Λ^2. We call Λ^2 the *master element*.

Domain $\hat{\Omega}$ is more of a convenient mathematical concept than a computational necessity. In actual applications, mappings can be carried out directly between Ω_e and the master element, Λ^2.

2.4. *Isoparametric Spectral Element Interpolation*

The basis functions used in the present work, $h_i(\xi)$, are the so-called Gauss–Lobatto–Legendre polynomials [17]. They are defined by

$$h_i(\xi)=-\frac{(1-\xi^2)L'_N(\xi)}{N(N+1)L_N(\xi_i)(\xi-\xi_i)} \qquad (i=0, 1, ..., N), \tag{2.18}$$

where L_N is the Nth-order Legendre polynomial, L'_N is its first derivative and the collocation point ξ_i

$(i=1, 2, ..., N-1)$ is the ith root of $L'_N(\xi)$ and $\xi_0 = -1$, $\xi_N = 1$.

By this definition we know that $h_i(\xi_j)$ is a Kronecker delta function, i.e.,

$$h_i(\xi_j) = \delta_{ij} \qquad \forall i, j \in \{1, 2, ..., N\}^2. \tag{2.19}$$

Then on the master element we give a basis set $\{\psi_{ln}\}$

$$\psi_{ln}(\xi, \eta) = h_l(\xi)\, h_n(\eta), \qquad l, n = \{0, 1, 2, ..., N\}^2. \tag{2.20}$$

With this basis set, we can define a mapping between Ω_e and the master element in the following tensor-product format:

$$(x, y) = (x_i, y_j)\, h_i(\xi)\, h_j(\eta). \tag{2.21}$$

Here we used the convention of tensor product that if a subscript is repeated it means a summation over all the components represented by that subscript. Similar convention of tensor product summation will be used in later parts of this paper. The above definition, in particular, sets a one-on-one mapping between the interpolation points (x_i, y_j) on the subdomain Ω_e and the Gauss–Lobatto points (ξ_i, η_j) on the master element, because $(x, y) = (x_i, y_j)$ when $(\xi, \eta) = (\xi_i, \eta_j)$.

Now the basis set $\{\psi_{ln}\}$ on the master element has its projection $\{\psi^e_{ln}\}$ on each subdomain Ω_e through the mapping (2.21) and

$$\psi^e_{ln}[(x, y) \mid (x, y) \in \Omega_e] = h_l[\xi(x, y)]\, h_n[\eta(x, y)], \qquad l, n = \{0, 1, 2, ..., N\}^2. \tag{2.22}$$

With well-distributed interpolation points on Ω_e, it can be proved that $\{\psi^e_{ln}\}$ is complete (when $N \to \infty$) and orthogonal. Therefore, if $\mathscr{M}^e$ is the subspace spanned by $\{\psi^e_{ln}\} \in \mathscr{H}^1$, then there is a projection Π_e such that $\forall u^e(x, y \mid x, y \in \Omega_e) \in \mathscr{H}^1$

$$\Pi_e(u^e(x, y)) = u^e_h(\xi(x, y), \eta(x, y)) \in \mathscr{M}^e, \tag{2.23}$$

where u^e_h is the numerical approximation of u^e.

Then, it follows that there is a projection Π such that $\forall u(x, y \mid x, y \in \Omega) \in \mathscr{H}^1$

$$\Pi[u(x, y)] = u_h = \bigcup_{e=1}^{K} u^e_h[\xi(x, y), \eta(x, y)] \in \bigcup_{e=1}^{K} \mathscr{M}^e, \tag{2.24}$$

where u_h is the numerical approximation of u by the piecewise polynomials, and

$$\bigcup_{e=1}^{K} u^e_h \to u \qquad \text{when} \quad N^2 \to \infty \qquad \text{or} \qquad \Delta_{\max} \to 0, \tag{2.25}$$

where N^2 is the dimension of $\mathscr{M}^e$ and $\Delta_{\max}$ is the maximum size of the subdomains Ω_e. Similar statements can be made for the case of $u(x, y \mid x, y \in \Omega) \in \mathscr{H}^1_0$ (the case with Dirichlet boundary condition).

Now we see that the spectral element method has two ways to achieve better numerical precision, i.e., by increasing the dimensions of the subspaces, N^2, and/or the number of the elements, K. It can be very flexible and the optimum choice for these two parameters depends on each individual problem to be solved. This flexibility of the spectral element method is one of its most attractive features compared with the spectral method and the finite element method.

Let the solutions of the shallow water equations at time t and the test functions on each subdomain Ω_e be expanded as

$$\begin{pmatrix} u^e(x, y, t) \\ v^e(x, y, t) \\ h^e(x, y, t) \\ \bar{u}^e(x, y) \\ \bar{v}^e(x, y) \\ \bar{h}^e(x, y) \end{pmatrix} = \begin{pmatrix} u^e_{ij}(t) \\ v^e_{ij}(t) \\ h^e_{ij}(t) \\ \bar{u}_{ij} \\ \bar{v}_{ij} \\ \bar{h}_{ij} \end{pmatrix} \psi^e_{ij}[\xi(x, y), \eta(x, y)], \tag{2.26}$$

where $f^e_{ij}(t)$ is the value of function f at the collocation point $(x_i, y_j) \in \Omega_e$ at time t. For the same basis set is used in mapping the coordinates and interpolating the solutions and test functions, it has been called the *isoparametric* method.

Since the test functions $\bar{u}$, $\bar{v}$, $\bar{h}$ are arbitrary, by substituting the expressions in (2.21) and (2.26) into the variational equations (2.13)–(2.15), we can derive the following tensor-product equation system

$$\sum_{e=1}^{K}{}' du^e_{ij}(t)/dt\, B^e_{ijrs} = -\sum_{e=1}^{K}{}' [F^e_{1ij}(t) - y^e_{ij} v^e_{ij}(t)]\, B^e_{ijrs} + \frac{1}{R_e} u^e_{ij}(t)\, A^e_{ijrs} \tag{2.27}$$

$$\sum_{e=1}^{K}{}' dv^e_{ij}(t)/dt\, B^e_{ijrs} = -\sum_{e=1}^{K}{}' [F^e_{2ij}(t) + y^e_{ij} u^e_{ij}(t)]\, B^e_{ijrs} + \frac{1}{R_e} v^e_{ij}(t)\, A^e_{ijrs} \tag{2.28}$$

$$\sum_{e=1}^{K}{}' dh^e_{ij}(t)/dt\, B^e_{ijrs} = \sum_{e=1}^{K}{}' u^e_{ij}(t)[h^e_{ij}(t) + 1]\, C^e_{ijrs} + v^e_{ij}(t)[h^e_{ij}(t) + 1]\, D^e_{ijrs}, \tag{2.29}$$

where the summation $\sum'$ is the direct stiffness matrix summation (assembling) as used in the finite element method [8] and

$$B^e_{ijrs} = \int_{A^2} \psi^e_{ij}(\xi, \eta)\, \psi^e_{rs}(\xi, \eta)\, |J^e(\xi, \eta)|\, d\xi\, d\eta \tag{2.30}$$

$$A^e_{ijrs} = \int_{A^2} \left[\frac{\partial \psi^e_{ij}(\xi, \eta)}{\partial x} \frac{\partial \psi^e_{rs}(\xi, \eta)}{\partial x} + \frac{\partial \psi^e_{ij}(\xi, \eta)}{\partial y} \frac{\partial \psi^e_{rs}(\xi, \eta)}{\partial y} \right] \times |J^e(\xi, \eta)|\, d\xi\, d\eta \tag{2.31}$$

$$C^e_{ijrs} = \int_{A^2} \frac{\partial \psi^e_{rs}(\xi, \eta)}{\partial x} \psi^e_{ij}(\xi, \eta)\, |J^e(\xi, \eta)|\, d\xi\, d\eta \tag{2.32}$$

$$D^e_{ijrs} = \int_{A^2} \frac{\partial \psi^e_{rs}(\xi, \eta)}{\partial y} \psi^e_{ij}(\xi, \eta)\, |J^e(\xi, \eta)|\, d\xi\, d\eta \tag{2.33}$$

$$F^e_{1ij}(t) = \frac{1}{2} [u^e_{mp}(t)]^2 \frac{\partial \psi^e_{mp}(\xi_i, \eta_j)}{\partial x} + v^e_{ij}(t)\, u^e_{mp}(t) \frac{\partial \psi^e_{mp}(\xi_i, \eta_j)}{\partial y} + h^e_{mp}(t) \frac{\partial \psi^e_{mp}(\xi_i, \eta_j)}{\partial x} \tag{2.34}$$

$$F^e_{2ij}(t) = \frac{1}{2} [v^e_{mp}(t)]^2 \frac{\partial \psi^e_{mp}(\xi_i, \eta_j)}{\partial y} + u^e_{ij}(t)\, v^e_{mp}(t) \frac{\partial \psi^e_{mp}(\xi_i, \eta_j)}{\partial x} + h^e_{mp}(t) \frac{\partial \psi^e_{mp}(\xi_i, \eta_j)}{\partial y} \tag{2.35}$$

$$J^e(\xi, \eta) = \frac{\partial x}{\partial \xi} \frac{\partial y}{\partial \eta} - \frac{\partial x}{\partial \eta} \frac{\partial y}{\partial \xi} \qquad (x,\ y \in \Omega_e). \tag{2.36}$$

All the integrations in the above equations are evaluated by the Gauss–Lobatto quadrature scheme, which is an exact formula for $(2N-1)$th-order polynomials. One advantage of using the Gauss–Lobatto–Legendre polynomials as basis functions is that we only have to deal with one set of grid points for both interpolating the solutions and evaluating the integrals.

The x and y derivatives in (2.31)–(2.35) can be expressed in terms of derivatives with local coordinates, ξ and η, according to the formulae

$$\begin{pmatrix} \dfrac{\partial}{\partial x} \\ \dfrac{\partial}{\partial y} \end{pmatrix} = \frac{1}{J^e} \begin{pmatrix} \dfrac{\partial y}{\partial \eta} & -\dfrac{\partial y}{\partial \xi} \\ -\dfrac{\partial x}{\partial \eta} & \dfrac{\partial x}{\partial \xi} \end{pmatrix} \begin{pmatrix} \dfrac{\partial}{\partial \xi} \\ \dfrac{\partial}{\partial \eta} \end{pmatrix}. \tag{2.37}$$

The matrix formulae of (2.27)–(2.29) are

$$[B][du(t)/dt] = -\{[F_1(t)] - [yv(t)]\}[B] - \frac{1}{R_e}[u(t)][A] \tag{2.38}$$

$$[B][dv(t)/dt] = -\{[F_2(t)] + [yu(t)]\}[B] - \frac{1}{R_e}[v(t)][A] \tag{2.39}$$

$$[B][dh(t)/dt] = \{[u(t)\, h(t)] + [u(t)]\}[C] + \{[v(t)\, h(t)] + [v(t)]\}[D], \tag{2.40}$$

where $[f(t)]$ is the vector whose components are the values of function $f(t)$ at all collocation points; and the global "stiffness matrices," i.e., $[A]$, $[B]$, $[C]$, and $[D]$, are obtained by the summations of the local "stiffness matrices," A^e, B^e, C^e, D^e, in the following format:

$$[G] = \sum_{e=1}^{K}{}' G^e. \tag{2.41}$$

When boundary condition (2.12) is imposed, the columns and rows corresponding to the boundary points should be eliminated from the matrices of (2.38) and (2.39) because u, v, $\bar{u}$, $\bar{v}$ vanish at those points.

2.5. *Temporal Discretization*

Since we consider viscous flow, the restriction on the time step of an explicit time marching scheme can be severe if the Reynolds number is small (A_H is large). We may improve this sitution by treating the nonlinear terms explicitly and the viscous terms implicitly [14].

In ocean applications, however, R_e is usually large ($O(10^2)$—$O(10^3)$). It has been shown [10, 11] that a large Reynolds number ($\sim O(10^3)$) is essential in maintaining strong wave–wave interactions in the western boundary region. When the Reynolds number is large, a fully explicit time discretization scheme is probably more practical. Here we use the third-order Adams–Bashforth time marching scheme for (2.38)–(2.40)

$$[B][u^{n+1}] = [B][u^n] - \Delta t \sum_{q=0}^{2} \alpha_q \{[F_1^{n-q}] - [yv^{n-q}]\}[B] + \frac{1}{R_e}[u^{n-q}][A] \tag{2.42}$$

$$[B][v^{n+1}] = [B][v^n] - \Delta t \sum_{q=0}^{2} \alpha_q \{[F_2^{n-q}] + [yu^{n-q}]\}[B] + \frac{1}{R_e}[v^{n-q}][A] \tag{2.43}$$

$$[B][h^{n+1}] = [B][h^n] + \Delta t \sum_{q=0}^{2} \alpha_q \{[u^{n-q}h^{n-q}] + [u^{n-q}]\}[C] + \{[v^{n-q}h^{n-q}] + [v^{n-q}]\}[D], \tag{2.44}$$

where $[f^n]$ is the value of $[f(t)]$ at time $t = n\,\Delta t$.

Figure 1 shows the stability regions for the four lowest order Adams–Bashforth schemes. We see that the stability region generally dwindles when the order of the method increases. However, for very large values of Reynolds number or fluid with very small viscosity, the third-order Adams–Bashforth scheme appears to be the best since it includes the most of the imaginary axis.

Using the Nth-order Legendre spectral element method with K elements, we calculated the eigenvalues of the advection operator

$$Lu = \frac{du}{dx}, \qquad x \in [-1, 1] \tag{2.45}$$

with the boundary condition

$$u(-1) = 0 \tag{2.46}$$

and the eigenvalues of the diffusion operator

$$Lu = \frac{d^2u}{dx^2}, \qquad x \in [-1, 1] \tag{2.47}$$

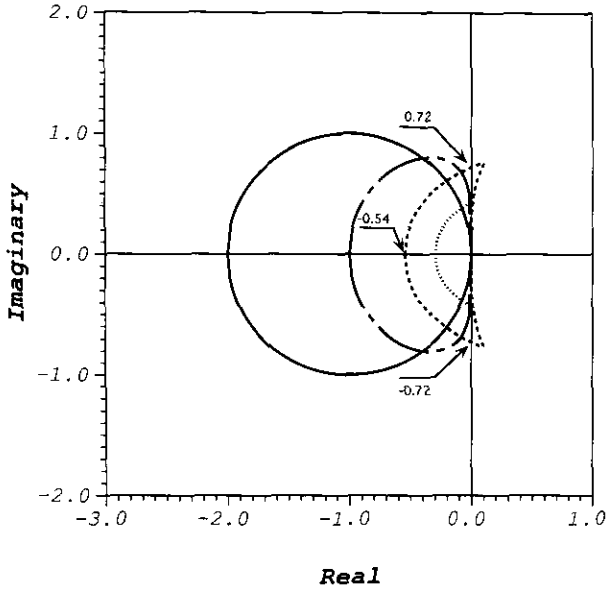

FIG. 1. Stability regions of the four lowest order Adams-Bashforth schemes. ——, first order; — — —, second order; – – –, third order; ···, fourth order.

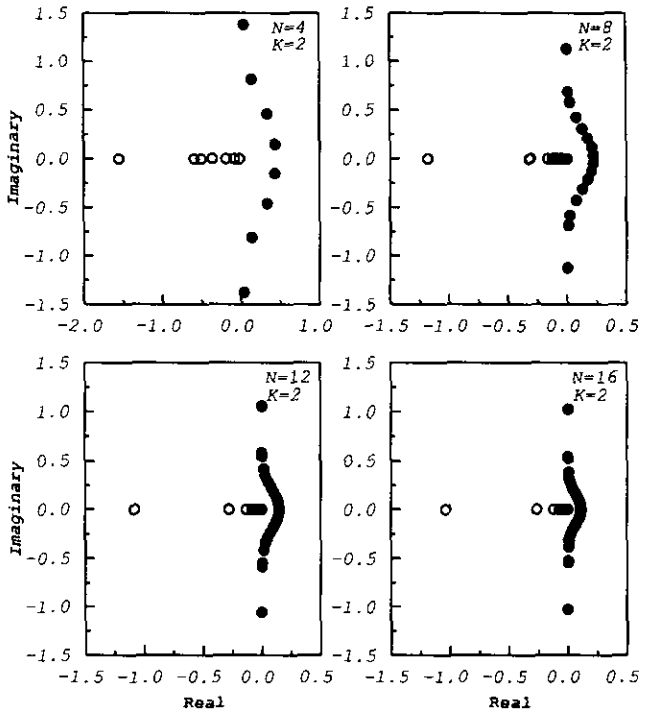

FIG. 2. Eigenvalues of the advection operator (2.45)–(2.46) divided by $N^2K/6$ (•), and those of the diffusion operator (2.47)–(2.48) divided by $N^4K^2/9$ (◦). These eigenvalues are calculated by the Legendre spectral element method. The elemental degrees of freedom is N and the element number is K.

with the boundary conditions

$$u(-1) = 0, \qquad u(1) = 0. \tag{2.48}$$

The numerical results show that when N becomes large, the maximum eigenvalues (in modulus) of the advection operator tend to have the magnitude of $N^2K/6$ and they are virtually on the imaginary axis (Fig. 2). For the diffusion operator, on the other hand, all its eigenvalues are real and negative, and the biggest one tends toward $-N^4K^2/9$ when N becomes large (Fig. 2). Hence, with the third-order Adams–Bashforth scheme, the stability restriction for an advection problem can be obtained as

$$\Delta t \leqslant 4.3/N^2K \tag{2.49}$$

and that for the diffusion problem would be

$$\Delta t \leqslant 4.8/N^4K^2. \tag{2.50}$$

These numbers only reflect the results on the computation domain of $[-1, 1]$, and they should be modified accordingly if a different size of domain is used.

Comparing to the Legendre collocation method [4], the maximum modulus of the eigenvalues of the spectral

TABLE I

Measured Maximum Time Step Δt Allowed by Eqs. (2.42)–(2.44) with Various Values of the Reynolds Number, R_e, and Various Elemental Degrees of Freedom in Each Spatial Direction, N

$1/R_e$	$N=4$	$N=8$	$N=12$	$N=16$
0.0	0.16	0.06	0.02	0.01
0.0005	0.16	0.06	0.02	0.01
0.005	0.16	0.06	0.02	0.01
0.05	0.16	0.02	0.005	0.002
0.5	0.03	0.003	0.0006	0.0002

Note. The computational domain is a rectangle, $[-\pi, \pi]^2$, and it has two evenly distributed elements in each spatial direction.

element method is about K times smaller for the advection operator and K^2 times smaller for the diffusion operator than those of the spectral method, if they use the same number of total collocation points and the elements are evenly distributed. This renders the spectral element method a larger time step in inverse proportion to the ratios of eigenvalues between the spectral element method and the spectral method; i.e., the spectral element method allows K times larger time step for the advection problem and K^2 times larger time step for the diffusion problem than the spectral method does under the conditions we just mentioned.

From the size of the time step point of view, we can draw a conclusion from (2.49) and (2.50) that a fully explicit scheme would not cost more if the Reynolds number is comparable to or larger than KN^2. This threshold, however, can be even lower if the actual computer time needed to solve the problem is considered since a semi-implicit scheme is more time consuming than an explicit one in each time step. Table I gives the experimented Δt_{max} for (2.42)–(2.44) with various elemental degrees of freedom in x (y) direction and various values of the Reynolds number. It shows that Δt_{max} is insensitive to the Reynolds number until it becomes sufficiently small. The stability condition, therefore, indeed rests on the advection terms when the Reynolds number is large.

3. TEST CASES

We have done a couple of test cases to check the correctness of the algorithms of the spectral element model for the shallow water equations. Comparisons between the spectral element numerical solutions and the analytical ones have been made.

The linear equatorial Kelvin wave is used as one of these tests. When the semi-periodic boundary conditions are imposed such that the world oceans are connected in the zonal direction, the inviscid, linear equatorial Kelvin wave is a constant phenomenon in terms of its spatial structure and its eastward traveling speed. Figure 3 give two spectral element mesh layouts with the same total degrees of freedom. Figures 4 and 5 show the convergence rates obtained under these spectral element interpolations. Although both cases have achieved an exponential convergence rate, the overall performance is better in the case with finer elements at lower latitudes. This result is due to the fact that the equatorial Kelvin wave is a low latitudinal phenomenon with most of its energy confined to the equatorial region. The difference between the results of these two cases diminishes when the number of total interpolation points becomes large enough that the wave is adequately resolved in both cases.

In the case of an equatorial basin, the equatorial Kelvin wave is going to encounter the eastern boundary at time $t = L$, where L is the distance between the Kelvin wave and the eastern boundary at $t = 0$ (Figs. 6a, b). After the Kelvin wave hit the eastern boundary and the wave reflection

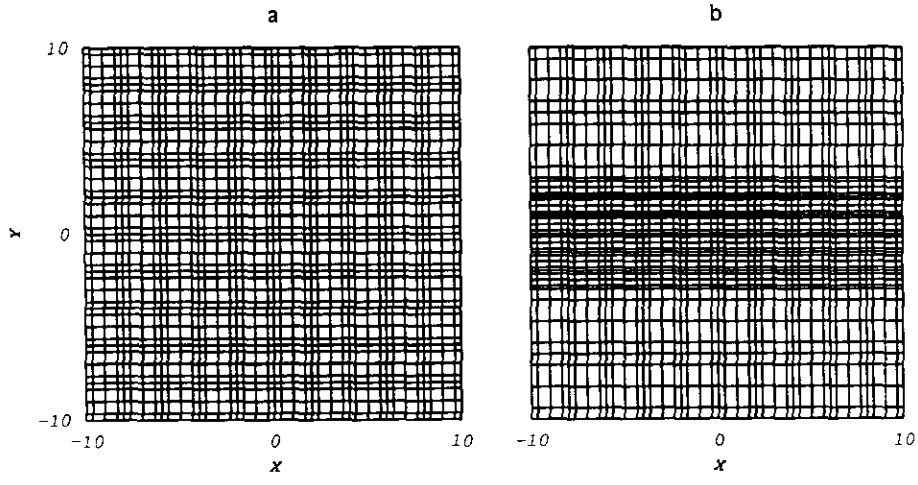

FIG. 3. Two example spectral element mesh layouts used in the equatorial Kelvin wave test case.

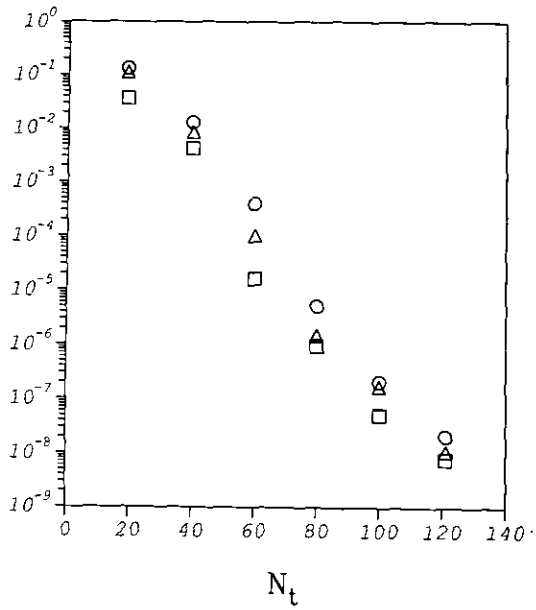

FIG. 4. The maximum pointwise error in the solution to the equatorial Kelvin wave with the same macro-element layout as that in Fig. 3a but with various total degrees of freedom in x or y directions, N_t. ○, $\|u-u_n\|$; □, $\|v-v_n\|$; △, $\|h-h_n\|$.

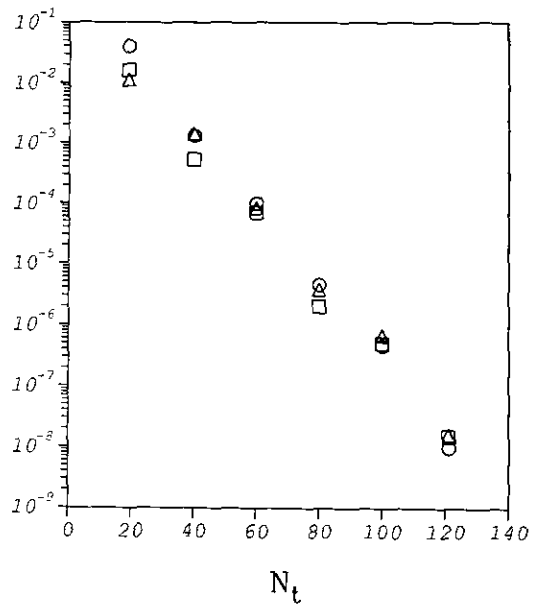

FIG. 5. The maximum pointwise error in the solution to the equatorial Kelvin wave with the same macro-element layout as that in Fig. 3b but with various total degrees of freedom in x or y directions, N_t. ○, $\|u-u_n\|$; □, $\|v-v_n\|$; △, $\|h-h_n\|$.

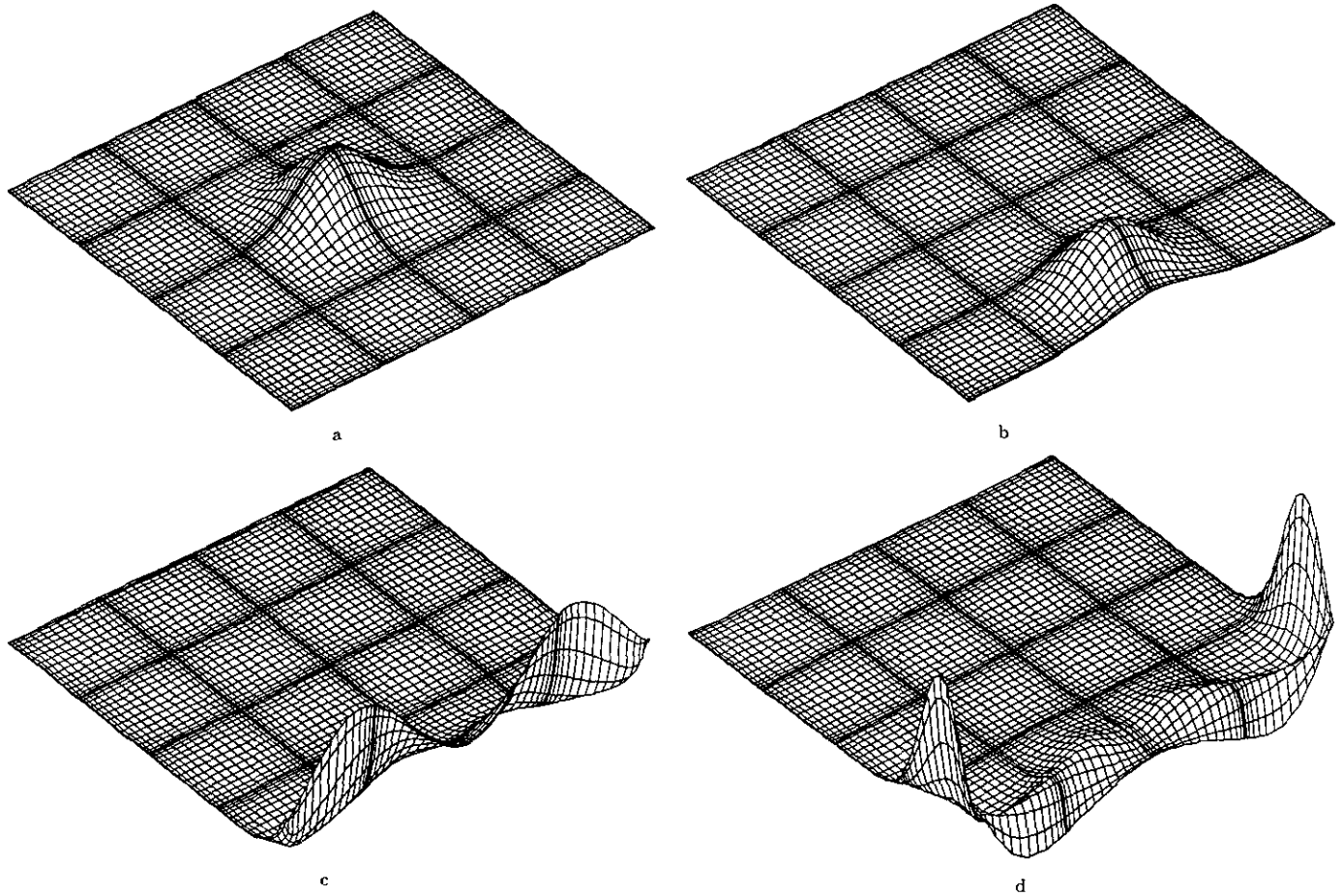

FIG. 6. (a) Surface plot of the initial equatorial Kelvin wave disturbance. Basin size: 10,000 km by 10,000 km (34 by 34 nondimensional units). (b) As Fig. 6a but at $t = 18.5$ days. (c) As Fig. 6a but at $t = 30.1$ days. (d) As Fig. 6a but at $t = 41.7$ days.

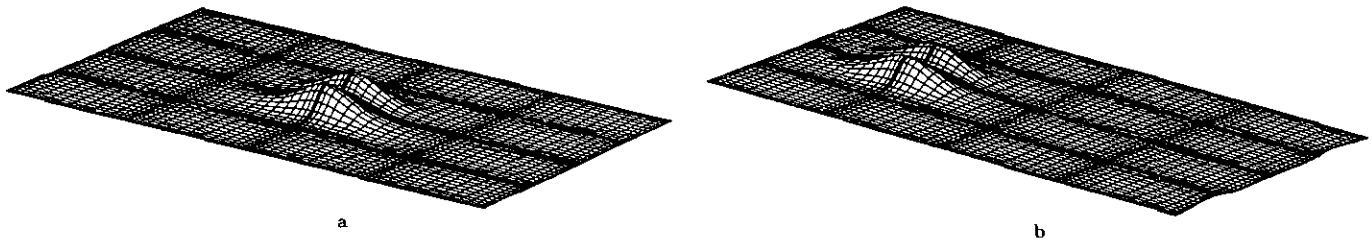

FIG. 7. (a) Surface plot of the initial equatorial solitary Rossby wave. Basin size: 10,000 by 5000 km (34 by 17 nondimensional units). (b) As Fig. 7a but at $t = 37.62$ days.

occurred, a major portion of the equatorial Kelvin wave splits into two poleward propagating coastal Kelvin wave components, each traveling in the opposite direction of the other (Fig. 6c). Eventually, both of them turn around the corners of the basin and return to the equator. Besides the coastal Kelvin waves, the reflection of the Kelvin wave at the eastern boundary also generates gravity waves and westward propagating Rossby waves (Fig. 6d). The above characteristics of the numerical solution are in good agreement with those predicted by the known equatorial wave theories [13]. We note that the surface plot in Fig. 6d is not very smooth, which indicates that the numerical precision is no longer very good after the time of the eastern boundary reflection. We need to refine the interpolation to resolve the shorter waves generated by the reflection of the Kelvin wave. A similar situation also occurred in the Rossby wave's reflection at the western boundary, but its extent is much worse. This problem will be dealt with in the next section.

Another test we have run for the spectral element model for the shallow water equations is to use the equatorial solitary Rossby wave (Rossby modon) solution [1] as the initial condition and then to compare the numerical result with the perturbation solution. Because of the balance between the weak nonlinearity and the weak dispersion, the perturbation solution predicts that the equatorial solitary Rossby wave should propagate to the west without changing its shape. The viscosity effect has to be excluded.

TABLE II

Computational Efficiency of the Spectral Element Model for the Shallow Water Equations ((2.42)–(2.44)) with a Rectangular Domain

Relative precision	Total degrees of freedom	Number of elements in x direction	Number of elements in y direction	Degrees of freedom per element	Cpu time per time step
1.0E-4	2145	4	2	256	0.95 s
1.0E-3	2145	8	4	64	0.71 s
5.0E-2	2145	16	8	16	0.52 s

Note. The relative precision (the absolute error divided by the amplitude of the solution) is estimated without the viscous terms, but they are included in other items of this table. Timings were measured on an Alliant-FX80 with vectorization.

At the beginning of the numerical integration, a small amount of the wave (about 4% of the initial amplitude) falls off the main water hump and travels to the east as equatorial Kelvin waves. This is because the initial condition is not an exact solution but contains some perturbation error. After 85 days (five nondimensional time units), the "true Rossby wave" part is well separated from the error part of the initial condition and the equatorial solitary Rossby wave keeps a permanent form (within the numerical precision of 10^{-4}) thereafter while it travels to the west (Figs. 7a, b), which is in agreement with Boyd's prediction [1]. The first-order perturbation approximation for the phase speed of the equatorial solitary Rossby wave is $-0.78\ \text{ms}^{-1}$, and the numerical solution yields a value of $-0.77\ \text{ms}^{-1}$. The corresponding linear Rossby wave phase speed is $-0.667\ \text{ms}^{-1}$. Therefore, the nonlinear effect has increased the phase speed of the equatorial Rossby wave with a positive sea surface displacement by almost 17%.

The computational efficiency of the spectral element model for the shallow water equation model is summarized in Table II. Without changing the total number of the interpolation points, using more elements in each direction reduces the computational cost, but at the same time, the precision level becomes lower; 12 to 16 degrees of freedom in each dimension of an element are needed to achieve spectral precision in the present study. How many elements should be used and how to distribute them depend on the individual problems. This is one of the flexibilities of the spectral element method. Owing to its potential in vectorization, along with other advantages it has, the spectral element model for the shallow water equations has enabled us to carry out a computationally intensive simulation of the equatorial Rossby modon's reflection process rather inexpensively. The numerical results of this simulation is going to be described in the next section.

4. APPLICATION TO THE ROSSBY MODON'S REFLECTION PROBLEM

If we let the Rossby modon propagate for a long time, the ocean boundary effect will eventually set in, no matter how wide the model ocean is. At that time, the perturbation

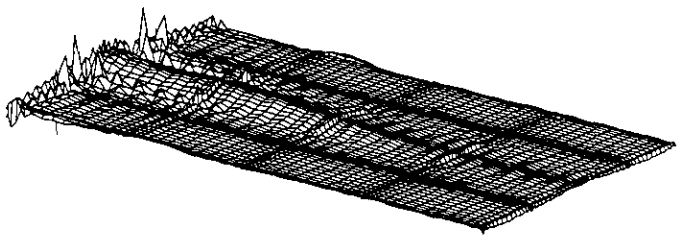

FIG. 8. As Fig. 7a but at $t = 90.1$ days. It shows that after the Rossby modon's reflection, unresolved short Rossby waves give rise to numerical instability.

solution is no longer valid. While the linear equatorial wave reflection theory has been developed for some time, the nonlinear scenario is still unknown to us. It would be interesting to numerically simulate the nonlinear reflection process and to see what would happen after the modon hits the western boundary.

In the last section, we have compared the numerical Rossby modon solution with the perturbation solution. Since the boundary effect was not our concern then, the relatively few evenly distributed spectral elements were able to produce a satisfactory result. However, the same spectral element interpolation could lead to numerical instability after the Rossby modon encountered the western boundary due to a lack of enough resolution in the western boundary region. The aliasing which resulted from the unresolved short Rossby waves eventually rendered the numerical integration meaningless (Fig. 8).

For the above reason, the spectral element interpolation is designed in such a way that it uses refined elements in the western boundary region in order to adequately resolve the turbulent reflection process there (Fig. 9). We have used fixed degrees of freedom for the basis functions so that the spectral interpolation grid on the *master element* is the same for every element. Since the current equatorial wave problem possesses pairity characteristics about the equator, only the solutions in the northern half of the 17×17 basin (~ 5000 km $\times$ 5000 km in dimensional units) need to be calculated, and those corresponding to the southern half can be reproduced according to their pairity properties. We have found that the higher the Reynolds number, the more turbulent is the flow in the western boundary region when the Rossby modon is reflected from there, and hence, the corresponding spectral element resolution should be finer in that region. Theoretically, lower Reynolds numbers generally mean smaller time steps, if a fully explicit model is used. In the present application we have found, however, that the smallest wavelength needed to be resolved is longer in a lower Reynolds number run than that in a high Reynolds number run, if the same precision level is required for both runs. Therefore, we may use a coarser spatial resolution for the lower Reynolds number run, which has the opposite effect on the restriction of the time step as that caused by the lower Reynolds number. The following simulation results are calculated with $\Delta t = 0.0025$ (6.12 min).

We first discuss the results with $R_e = 2000$ ($A_H = 2.9 * 10^6$ cm^2 s^{-1}). After the Rossby modon propagates westward for a time period of $t = 10$, it impinges on the western boundary and the major reflection process begins (Figs. 10a, b). It is very interesting to observe that the nonlinear effect not only causes the overshooting in the north–south (poleward) direction in the western boundary layer (Fig. 10c), but it also stimulates the formation of the multiple vortices there (Fig. 10d). The linear theory predicts, however, that if we count the number of vortices in the north–south (y) direction, that there should be only one vortex on each side of the equator after the Rossby modon's reflection. Moreover, the vortices created in a strongly nonlinear reflection process

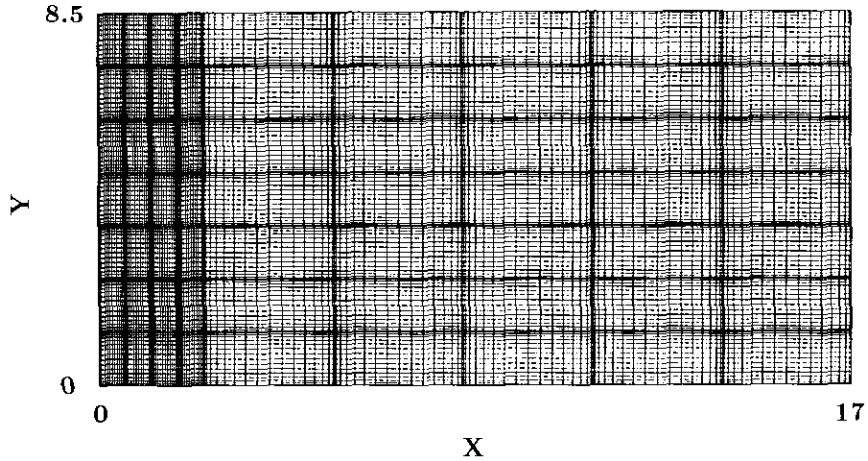

FIG. 9. The northern half of the spectral element mesh used in simulating the Rossby modon's reflection in a rectangular basin. The physical problem has symmetrical properties about the equator, so only the solutions in the northern half of the basin need to be calculated.

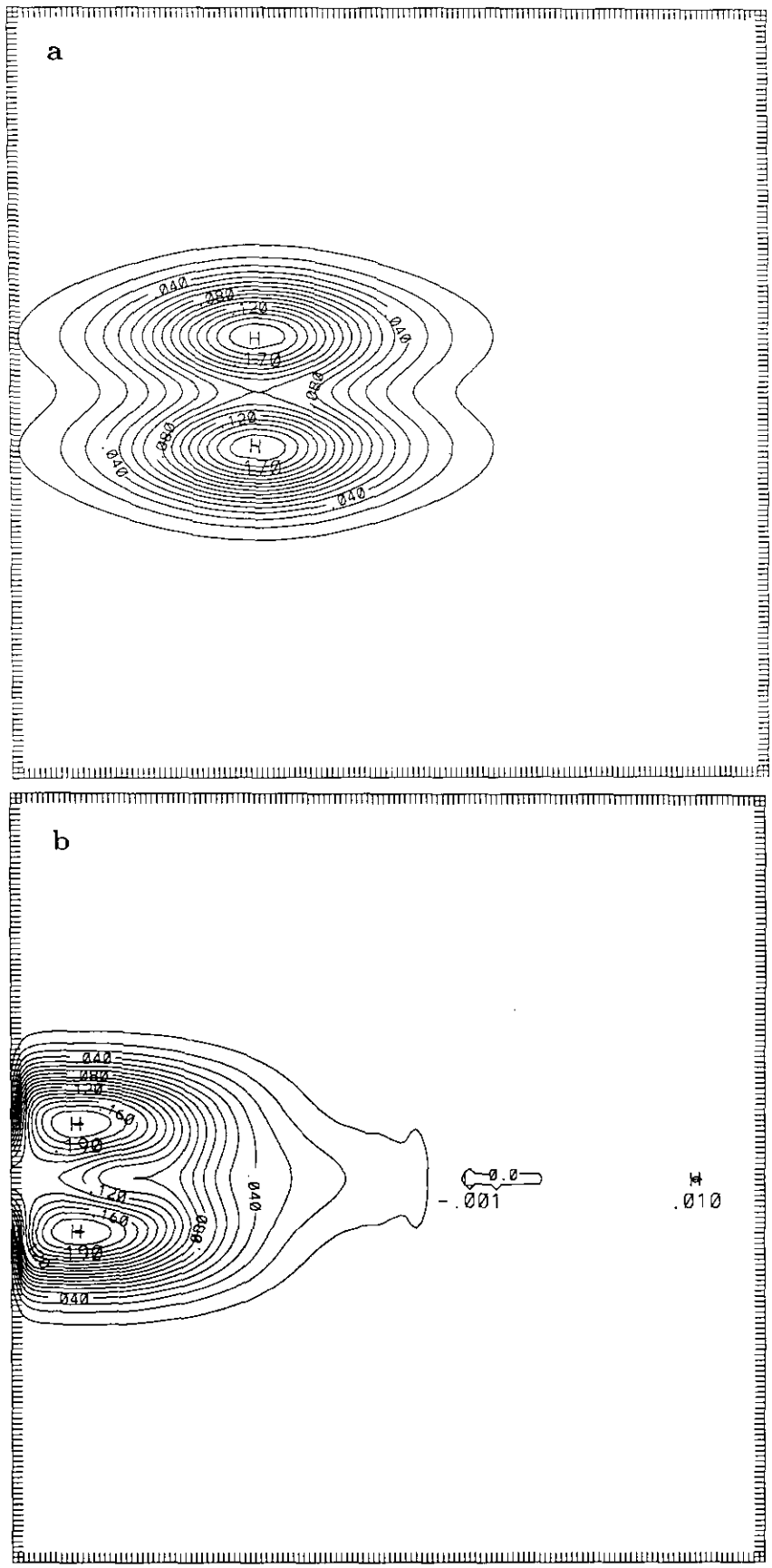

FIG. 10. (a) Contour plot of the upper layer thickness displacement due to the initial Rossby modon. $R_c = 2000$. Contour interval = 0.01. (b) As Fig. 10a but at $t = 10$. (c) As Fig. 10a but at $t = 20$. (d) As Fig. 10a but at $t = 40$. Labels scaled by 1000.

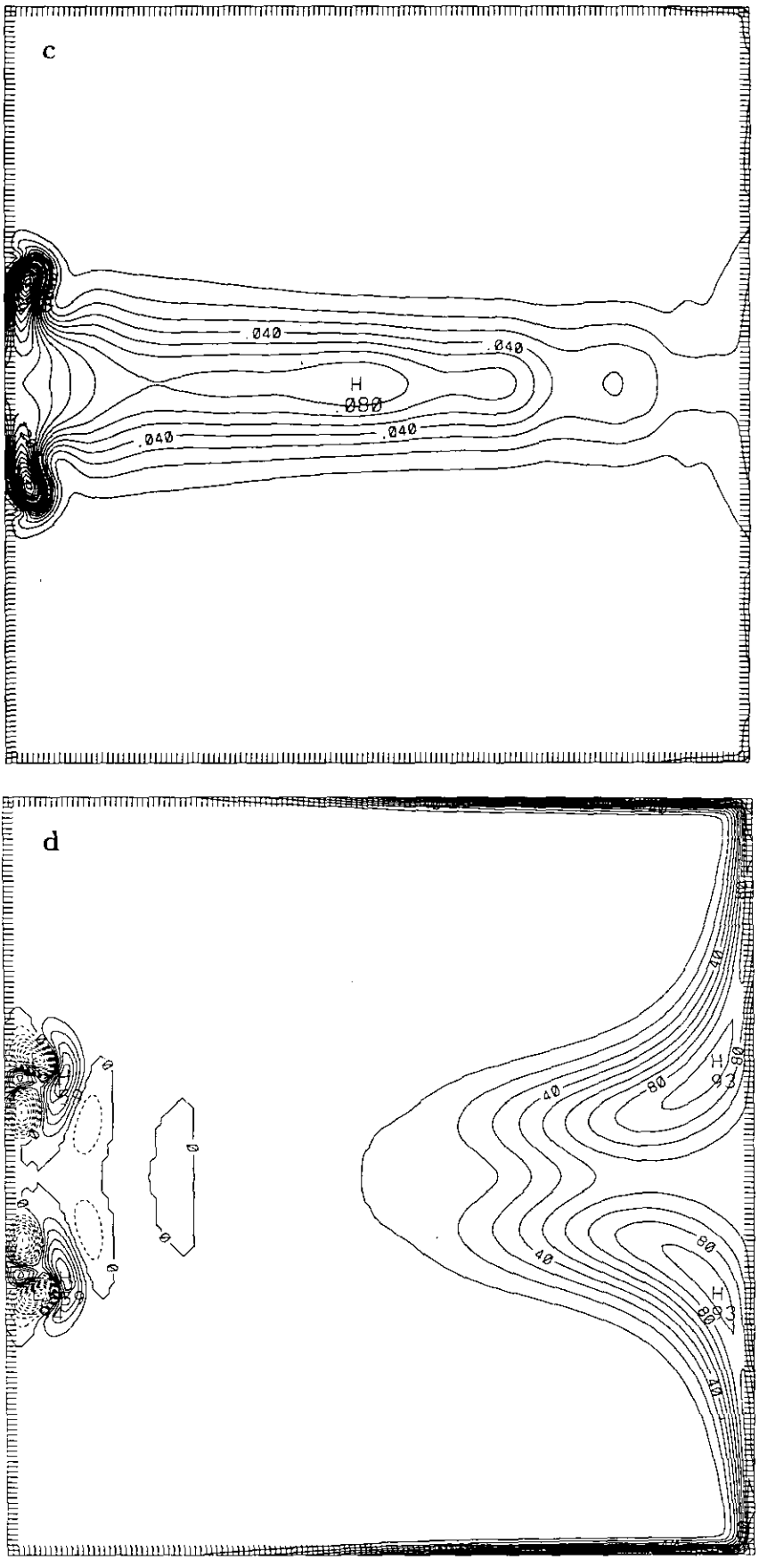

FIG. 10—*Continued.*

are much more energetic than those in a linear reflection process [11]. The eddies created in the strongly nonlinear reflection process in the western boundary region are typically of sizes from 200 to 600 km in diameter (Figs. 11a, b).

Besides the short Rossby waves confined in the western boundary region, a major portion of the Rossby modon's energy is transferred into eastward propagating Kelvin waves by the reflection. Later, these Kelvin waves arrive at the eastern boundary and are reflected from there (Fig. 10d). Since the difference between the wavelengths of the incident and the reflected waves in the eastern boundary region is not nearly as drastic as in the western boundary region and the waves in the east are relatively long waves, we are able to obtain smooth solutions even though we have used far less spectral element interpolation outside the western boundary region.

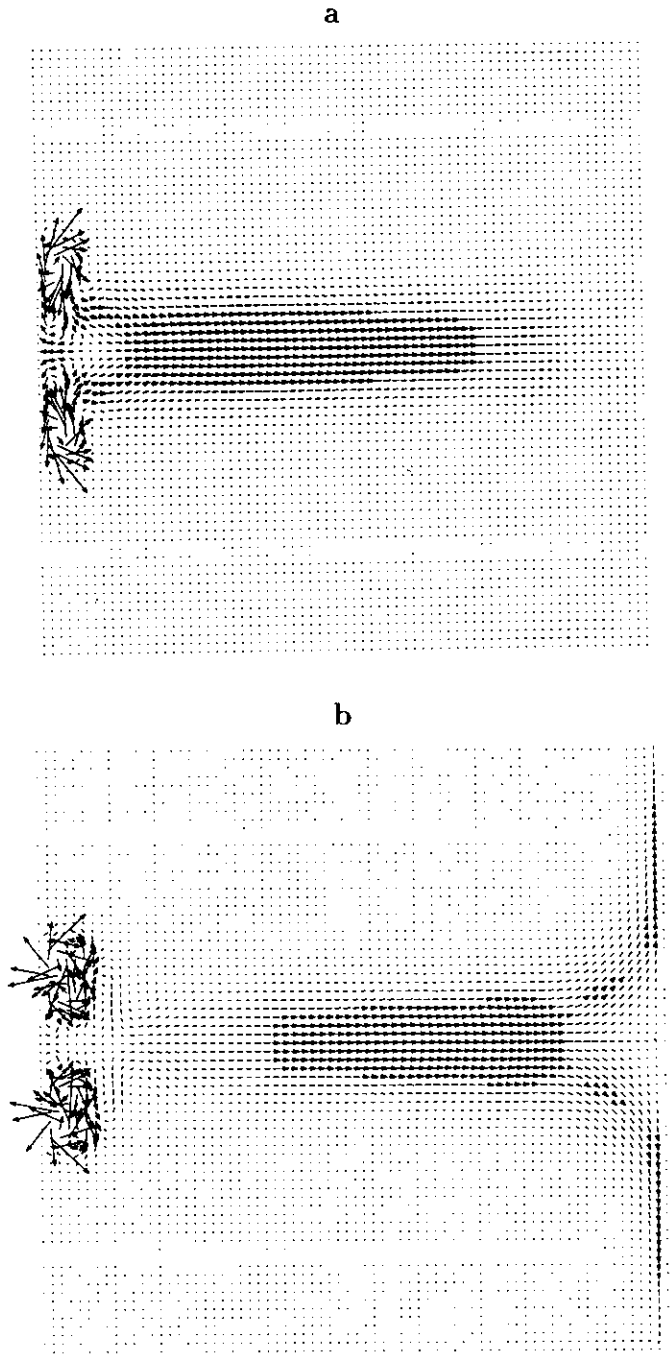

FIG. 11. (a) Velocity field at $t = 20$. (b) As Fig. 10a at $t = 30$.

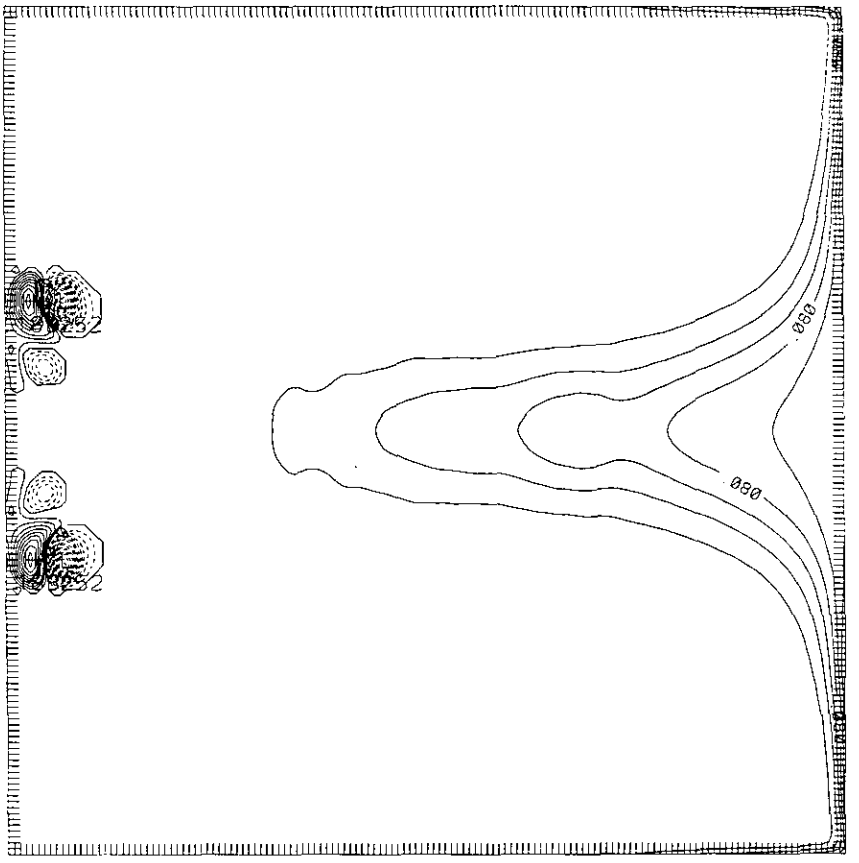

FIG. 12. Contour plot of the upper layer thickness displacement with $R_e = 10000$; $t = 30$ and contour interval = 0.02.

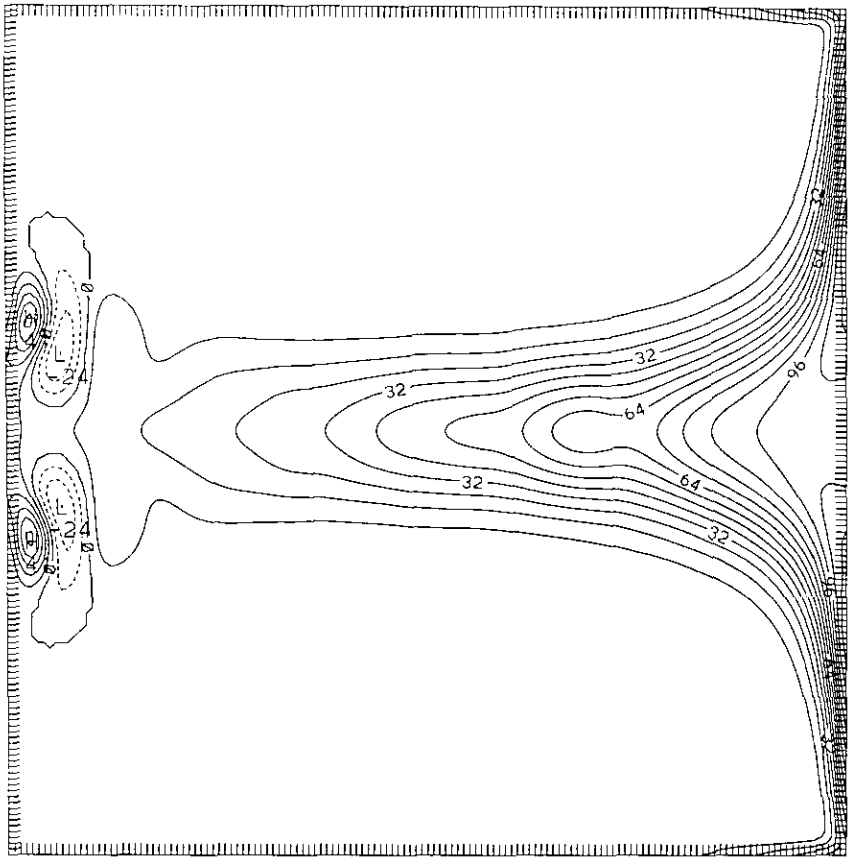

FIG. 13. Contour plot of the upper layer thickness displacement with $R_e = 200$; $t = 30$, contour interval = 0.008, and labels scaled by 1000.

We repeated the simulation with different values of R_e. It is found that the vortex activities in the central western boundary region are very sensitive to this parameter. With $R_e = 10{,}000$ ($A_H = 5.8 * 10^5\ cm^2\ s^{-1}$), the eddies there become more energetic compared to the rest of the ocean (Fig. 12) much more so than those with $R_e = 2000$. Another impressive phenomenon with this larger Reynolds number is that the vortex pair system in the western boundary region shows an interesting anticyclonic rotation about its center [11]. In the case of $R_e = 200$ ($A_H = 2.9 * 10^7 cm^2 s^{-1}$), however, the eddy phenomenon is not outstanding at all. The strength of the short Rossby waves in the western boundary region in the low Reynolds number case is comparable to that of the long waves in the rest of the ocean. Moreover, the meridional wave number of the dominant mode in the western boundary region has not been increased due to the reflection (Fig. 13), which is in agreement with the linear equatorial wave reflection theory [13].

Numerical simulations with realistic ocean boundary shapes have also been carried out. Figure 14 is a spectral element mesh for the Atlantic Ocean, which is designed to study the equatorial dynamics. This figure is stretched in the y direction to show the finer elements in low latitudes where the energy of the equatorial waves is trapped. The zonal lengths of the elements near the western boundary region are generally smaller than those in the eastern part of the ocean, for the same reasons as explained before. Figure 15 is a snapshot of the upper-layer thickness displacement in the simulation of the response of the Atlantic Ocean to the Rossby modon. Under the realistic geometry of the Atlantic Ocean, a train of eddies were generated in the northern equatorial region, which consumed a significant part of the energy carried by the original Rossby wave packet.

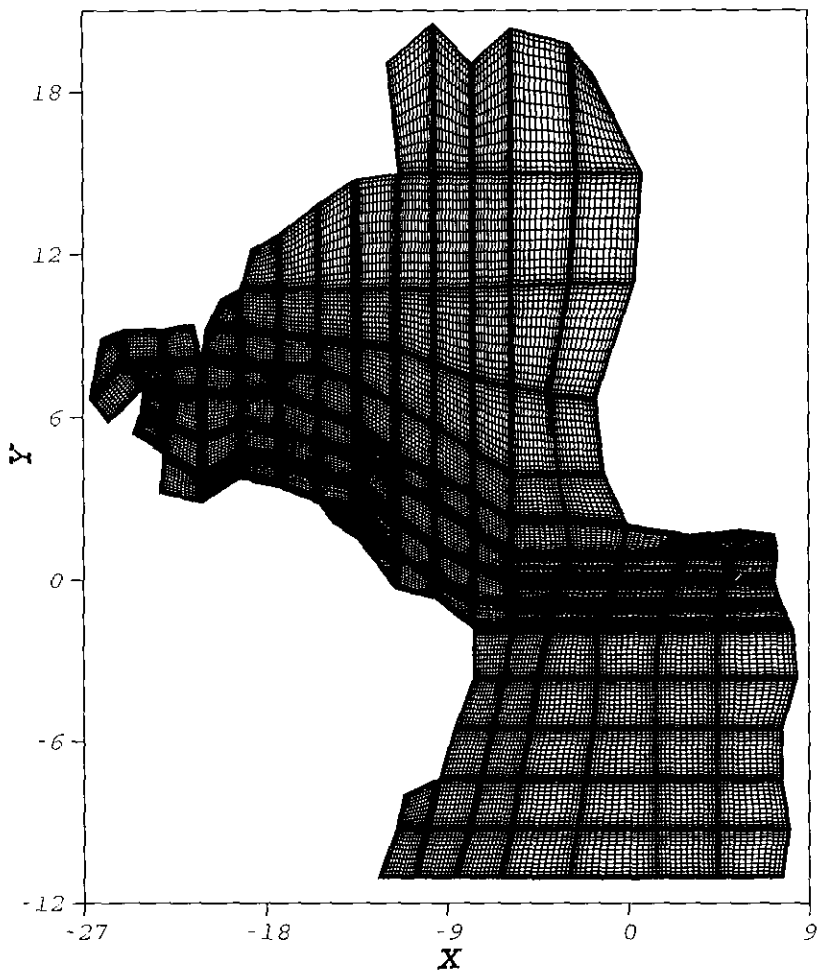

FIG. 14. The spectral element mesh for the Atlantic Ocean. The figure is stretched in the y direction to show the finer elements in the lower latitudes.

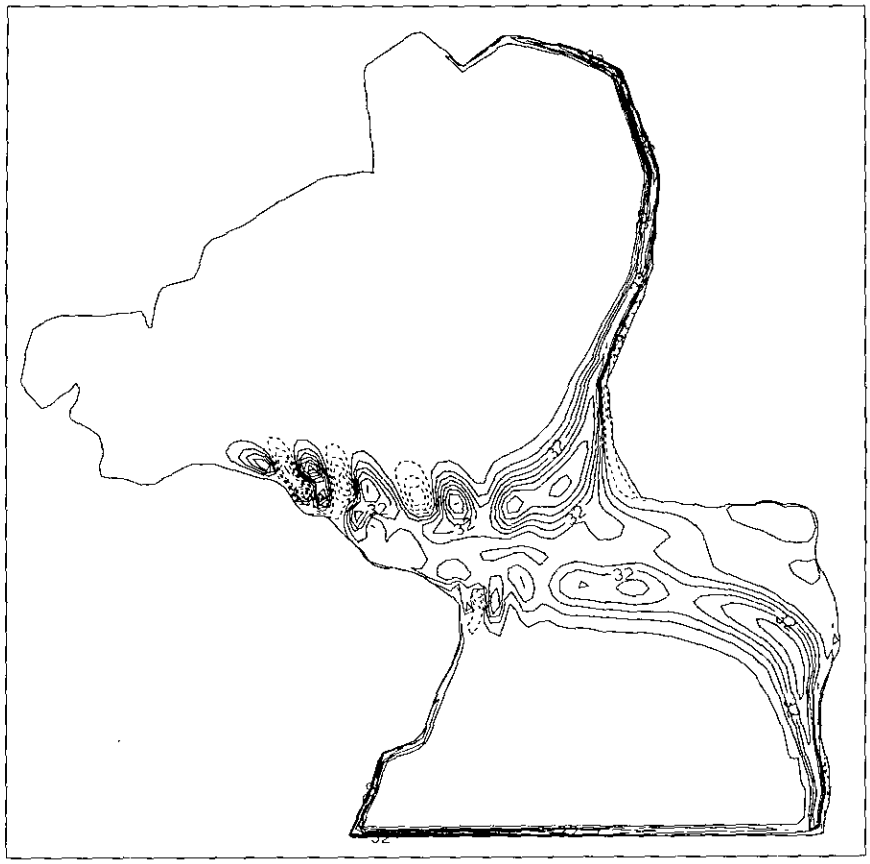

FIG. 15. Contour plot of the upper layer thickness displacement in the simulation of the Atlantic Ocean's response to a Rossby wave packet; $t = 70$, $R_e = 2000$, contour interval = 0.009, and labels scaled by 1000.

5. CONCLUSIONS

The spectral element model for the shallow water equations is constructed. It is shown that this model has the potential to solve oceanic problems efficiently. In particular, its flexibility in arranging the spectral elements and the fact that it is a high order numerical method make it a powerful tool for studying frontal phenomena in oceans. As an example, the equatorial Rossby modon's reflection problem is studied. We find that with high Reynolds numbers, the reflection of the Rossby modon can result in multiple energetic vortices in the western boundary region. The reflection with low Reynolds number causes much weaker eddy activities and the results are similar to those of the linear equatorial wave theory.

ACKNOWLEDGMENTS

An important part of this work is based on the Part I of the author's Ph.D. dissertation. The author wishes to express her gratitude to her thesis advisor, Professor John P. Boyd, for continued discussion and help; to Professor Guy A. Meadows and Professor William W. Schultz for many helpful discussions; to Roque Oliveira for assistance in using the Alliant FX80. This work received support from The National Science Foundation through Grants OCE8509923, OCE8812300, and DMS8716766; and from The Department of Atmospheric, Oceanic, and Space Sciences of The University of Michigan.

REFERENCES

1. J. P. Boyd, *J. Phys. Oceanogr.* **15**, 46 (1985).
2. J. P. Boyd, *Chebyshev and Fourier Spectral Methods* (Springer-Verlag, Heidelberg, 1989).
3. K. Bryan, *J. Atmos. Sci.* **20**, 594 (1963).
4. C. Canuto, M. Y. Hussaini, A. Quarteroni, and T. A. Zang, *Spectral Methods in Fluid Dynamics* (Springer-Verlag, New York, 1988).
5. P. F. Fischer and A. T. Patera, *J. Comput. Phys.* **92**, 380 (1991).
6. D. Gottlieb and S. A. Orszag, *Numerical Analysis of Spectral Methods: Theory and Applications* (SIAM, Philadelphia, 1977).
7. D. B. Haidvogel, A. R. Robinson, and E. E. Schulman, *J. Comput. Phys.* **34**, 1 (1980).
8. N. Kikuchi, *Finite Element Methods* (Cambridge Univ. Press, Cambridge, UK, 1986).

9. K. Z. Korczak and A. T. Patera, *J. Comput. Phys.* **62**, 361 (1986).
10. H. Ma, Ph.D. thesis, The University of Michigan, Ann Arbor, MI, 1991.
11. H. Ma, *J. Mar. Res.* **50**, 567 (1992).
12. Y. Maday and A. T. Patera, *State-Of-The-Art Surveys on Computational Mechanics 71–143*, edited by A. D. Noor and J. T. Oden (1989).
13. D. W. Moore and S. G. H. Philander, *The Sea* **6**, 319 (1977).
14. A. T. Patera, *J. Comput. Phys.* **54**, 468 (1984).
15. R. Peyret and T. Taylor, *Computational Methods for Fluid Flow* (Springer-Verlag, Heidelberg, 1986).
16. L. F. Richardson, *Weater Prediction by Numerical Process* (Cambridge Univ. Press, London/New York, 1922).
17. E. M. Ronquist, Ph.D. thesis, The Massachusetts Institute of Technology, 1988.
18. W. C. Thacker, A. Gonzalez, and G. E. Putland, *J. Comput. Phys.* **37**, 371 (1980).